Computers in Biology and Medicine 146 (2022) 105358

Contents lists available at ScienceDirect

Computers in Biology and Medicine

journal homepage: www.elsevier.com/locate/compbiomed

Comparison of ultrasound vector flow imaging and CFD simulations with PIV measurements of flow in a left ventricular outflow trackt phantom - Implications for clinical use and in silico studies

Paul Roger Leinan [a,*], Thomas Grønli [c], Paal Skjetne [a], Morten Smedsrud Wigen [c], Stig Urheim [d,e], Lasse Lovstakken [c], Sigrid K. Dahl [b]

[a] Department of Process Technology, SINTEF Industry, Trondheim, Norway
[b] Department of Health, SINTEF Digital, Trondheim, Norway
[c] Centre for Innovative Ultrasound Solutions, Dept. Circulation and Medical Imaging, Norwegian University of Science and Technology, Trondheim, Norway
[d] Department of Heart Disease, Haukeland University Hospital, Bergen, Norway
[e] Norway and University of Bergen, Clinical Institute 2, Bergen, Norway

ARTICLE INFO

Keywords:
US VFI
PIV
CFD
Validation
In silico modelling
Pulsatile flow

ABSTRACT

In this study we have compared two modalities for flow quantification from measurement data; ultrasound (US) and shadow particle image velocimetry (PIV), and a flow simulation model using computational fluid dynamics (CFD). For the comparison we have used an idealized Quasi-2D phantom of the human left ventricular outflow tract (LVOT). The PIV data will serve as a reference for the true flow field in our setup. Furthermore, the US vector flow imaging (VFI) data has been post processed with model-based regularization developed to both smooth noise and sharpen physical flow features. The US VFI flow reconstruction results in an underestimation of the flow velocity magnitude compared to PIV and CFD. The CFD results coincide very well with the PIV flow field maximum velocities and curl intensity, as well as with the detailed vortex structure, however, this correspondence is subject to exact boundary conditions.

1. Introduction

A challenge in bringing decision support systems based on in silico flow simulations into clinical use, is to achieve an adequate validation of the simulation models. Especially in the in-vivo setting there is an unmet need for methods to validate blood flow simulations, and there is currently no method which offers precise dynamic flow velocity quantification in 2D or 3D. Doppler ultrasound (US) can provide valid velocity estimates in real time, but only in the direction of the US beam path. MRI flow measures offer the possibility of 3D dynamic flow quantification, but for confident velocity estimates averaging over several heart cycles is needed. However, promising methods are under development, such as US vector flow imaging (VFI) and resent advances in 4D MRI flow are encouraging [1,2,3]. Nonetheless, there are still questions about the level of uncertainty in these measurement techniques, especially in an uncontrolled in-vivo setting, that makes it challenging to use them to validate numerical flow calculations in clinical practice. In this study, we have compared two modalities for flow quantification from measurement data; ultrasound and shadow particle image velocimetry (PIV), and one flow simulation model using computational fluid dynamics (CFD). Hence, in our study, the ultrasound velocity reconstruction represent a flow validation tool that can be used to validate simulation models (e.g. CFD models) in an in-vivo setting. For the comparison we have used an idealized Quasi-2D phantom of the human left ventricular outflow tract (LVOT) [4]. The LVOT phantom has a known geometry and is connected to a mock cardiac flow loop where exact flow boundary conditions can be prescribed. The phantom is constructed to enable visual access for both US, through a soft material boundary (PVA hydrogel [5]), and PIV, such that simultaneous US and PIV recordings can be obtained.

Studies on experimental validation of computational biomedical flow models have been performed by several authors where CFD models have been compared and validated against MRI [6,7]; US [2,7,8,9,10]; PIV [11–13,6,14,15] and laser Doppler velocimetry [16,17]. A general error/uncertainty quantification is discussed in Refs. [18,19]. Additionally, segmented MRI and US data have in some studies been used to

* Corresponding author.
E-mail address: paul.roger.leinan@sintef.no (P.R. Leinan).

https://doi.org/10.1016/j.compbiomed.2022.105358
Received 8 September 2021; Received in revised form 10 February 2022; Accepted 25 February 2022
Available online 1 April 2022
0010-4825/© 2022 The Authors. Published by Elsevier Ltd. This is an open access article under the CC BY license (http://creativecommons.org/licenses/by/4.0/).

define the boundary conditions of the flow model [6,7], which is an essential capability for future clinical use of computational models, especially when patient specific models are considered and in the cases where the deformation of the solid boundaries are of importance to the results such as in the chambers of the hearth [20]. In a controlled in-vitro laboratory setting, a high quality data basis for validation of computational biomedical flow models both with deforming non-slip boundaries and with pulsatile flow can be achieved with laser PIV systems [21,22,23]. However, in a clinical setting the data basis, e.g. from US or MRI, for defining boundary conditions (both fluid and solid) are in most cases restricted both spatially and temporally because of technological and inherent limitations in the measurement techniques, such as the pulse length versus penetration depth which limits spatial resolution in medical US. Furthermore, the level of uncertainty in the measurement data are difficult to control and quantify because of the complexity and sample variation of biological structures. The goal of our current work is therefore to gain understanding and put focus on the challenges outlined above, namely, implications of measurement limitations and their biases when employed as a data basis for computational modeling in an in-vivo setting. To investigate this we have compared measurement techniques which have different strengths and usability in the in-vivo and in the in-vitro settings (US and PIV, respectively), and performed measurements and computational modeling (CFD) of the same biological relevant flow in a controlled but challenging laboratory flow phantom both seen from a measurement and modeling standpoint.

The primary variables of the flow field are the flow velocity components. Ultrasound VFI uses Doppler shift and speckle tracing to estimate the flow velocity components and PIV uses window correlation of particle images pairs. In CFD, the Navier–Stokes equations are solved numerically on a computational grid for the flow velocity components in addition to the pressure field. CFD is therefore a mathematical representation of the flow field based on conservation of mass and momentum subject to boundary conditions for the computational domain. Hence, for CFD to represent a physical case satisfactorily, a very detailed case specific geometry description and boundary conditions are required, which is challenging to achieve even in a controlled laboratory setting. In our laboratory setup we place most confidence in the velocity components calculated given by the PIV measurements, since they are derived from displacement analysis by cross-correlation of high quality image pairs of the flow spaced closely in time. Bias errors and other sources of uncertainty exists in PIV analysis [24], however, they will be less pronounced in our case than for results obtained for VFI. Hence, the PIV results will serve as a reference for the flow field in our analysis.

The VFI results have in this work been post processed with model-based (see 2.3) regularization developed to both smooth noise and sharpen physical flow features. This US VFI technique has shown promise for measuring the intrinsic intracardiac flow patterns, but challenges with measurement variance and dropouts remain. Hence, the use of VFI to validate numerical flow calculations is a challenge as long as there are a non-quantified biases in the regularized VFI results.

Our group have previously developed and tested an experimental quasi 2D flow model for studying pulsatile blood flow in the human left ventricular outflow tract (LVOT) and the ascending aorta (AAo) using shadow PIV [4], and achieved fair agreement between the CFD calculations and shadow PIV results. In the current work, we have employed the same experimental setup as in our previous work, however, modified it to enable simultaneous synchronized recordings of ultrasound VFI and shadow PIV.

Given the methodical differences in VFI, PIV and CFD, our results show that there are generally good agreements between the three modalities, especially when integrated quantities of the flow are compared, such as volumetric flow rate and flow field maximum velocities. However, the VFI flow reconstruction results in an underestimation of the flow velocity magnitude compared to PIV and CFD. The CFD results coincide well with PIV flow field maximum velocities and curl intensity. The detailed in plane vortex structure of the flow field deviates to some extents compared to the PIV results, however, the main vortex structure is well represented in the CFD results when compared to PIV and VFI. The main biases evident in the regularized VFI data when compared to PIV and CFD are, *i*) smoothing of the flow field producing less sharp velocity gradients; and *ii*) some imbalance between the velocity components tangential and normal to US probe when compared to PIV and CFD.

2. Methods

The geometry of the LVOT was acquired from 3D transthoracic echocardiography of a healthy female with consecutive segmentation of the endocardial wall [20]. The pulsatile inflow boundary condition used in the experiment was generated directly from the same recordings. The pulse rate in the recordings was 60 beats per minute (bpm). To provoke a complex pathological flow in the LVOT, the anterior mitral leaflet was adjusted to have a pronounced billowing (see Ref. [4] for details). A non-deformable geometry was assumed, and the chosen geometrical snapshot of the cardiac cycle represents peak systole when the aortic leaflets are fully open. The measurements in this study is therefore from the systolic period of the cardiac cycle.

The primary aim of this work is to compare modalities for flow quantification; regularized US, PIV and a CFD model aimed at biomedical applications and especially cardiac flows. A suitable flow scenario is needed for this comparison; however it is not a requirement that this flow scenario is biologically relevant. In spite of this, we chose a flow scenario that included some of the challenges and characteristic seen in cardiac flow, e.g., dynamic pulsatile flow with a complex vortex structure and relevant flow velocity magnitudes. Other characteristic of cardiac flows such as moving/deforming walls and vales, and non-Newtonian fluid properties were not included in our study. Hence our study is not aimed at advancing the knowledge of cardiac flows and pathologies of the cardiovascular system.

2.1. Experimental setup

The LVOT in-vitro model is designed to facilitate simultaneous US and PIV recordings. This is achieved by a molded Polyvinyl alcohol (PVA) plate sandwiched between two Plexiglas plates for visual access, as seen in Fig. 1. A 2D slice representation of LVOT is molded into the PVA plate, and becomes the fluid “flow volume” of the phantom. The thickness of the 2D LVOT slice is 7 mm. The two Plexiglas plates enclose the flow volume in the PVA plate and provides a water tight seal. Inlet and outlet ports (with an inner diameter of 15 mm) are attached to the back-end of the Plexiglas plate. Fluid is pumped through the phantom by a piston pump, which is controlled by programmable linear actuator (Zaber, X-LRQ-E) such that a given flow pulse could be injected into the phantom by displacement control. Fiber reinforced 1” transparent PVC tubing and two ball valves (SXE PVC-U, 1”) ensures unidirectional pulsatile flow through the setup. The flow loop is connected to a reservoir tank where polymer particles can be added as PIV tracers.

The PVA plate is US compatible, hence the US transducer can be placed on and in contact with the lip of the PVA plate (Fig. 1) and transmit and receive sound waves through the PVA plate and into the flow volume. The PVA material is made to match the speed of sound in water, 1500 m/s, and have an attenuation (0.54 dB/cm/MHz at 10.0 MHz) comparable to soft tissue.

Tap water at room temperature is used as flow medium in the experiments.

2.2. Shadow PIV

In order to obtain a high confidence measurement of the velocity field in the 2D plane of the LVOT phantom we use the particle shadow velocity technique. In the shadow PIV technique, a strong back-light is used inline with the measurement area and a high speed camera. Tracer

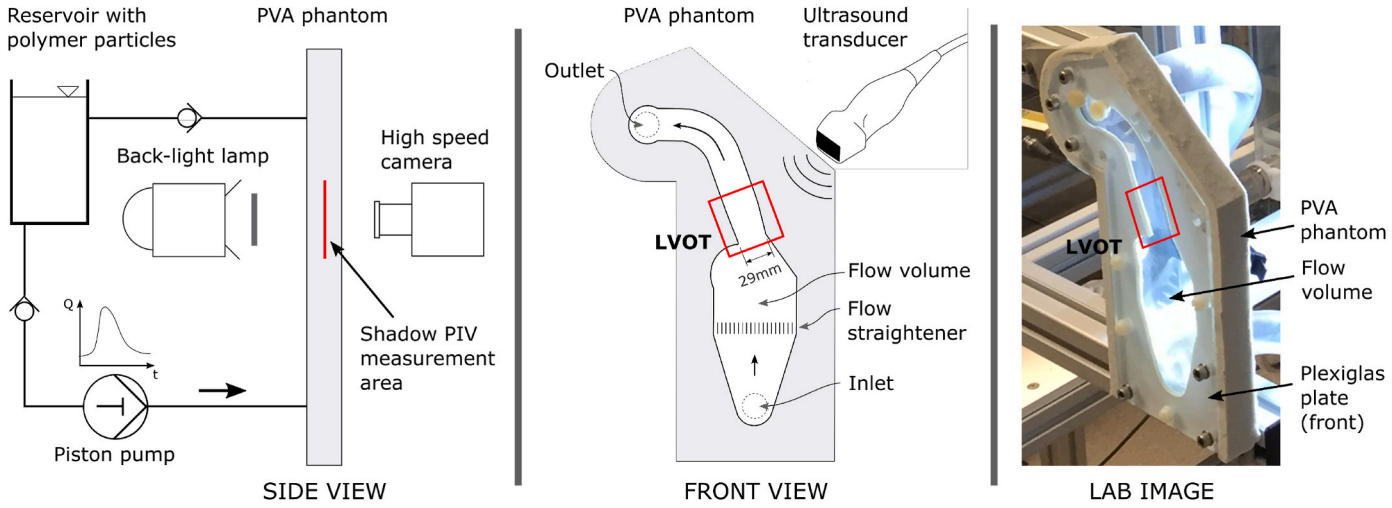

Fig. 1. Illustration of the experimental setup, which consists of a fluid reservoir, the 2D LVOT flow model, a piston pump, a linear actuator (Zaber, X-LRQ-E) and connecting fiber reinforced 1" tubes and one-way polymer ball valves (SXE PVC-U, 1"). Fluid can be pumped through the loop and the LVOT model in a pulsatile manner, determined by the waveform given to the linear actuator. The flow field in the 2D LVOT model was visualized by tracking the movement of polymer particles by recording their shadows projection with a high-speed camera (Photron FASTCAM Mini AX 200). The particle shadows where projected into the camera from a spot-light lamp (dedolight DLH400DT) and a light diffuser plate inline with a the camera.

particles are added to the fluid, which by the correct alignment and position of the back-light, measurement area and the high speed camera produces PIV images where the particles appears as shadows in the flow [25]. In our case a spot-light lamp (dedolight DLH400DT) is used for back-light illumination, additionally a light diffuser plate is placed between the back light and the flow measurement area. Images of the LVOT flow field with particle shadows is captured by a high-speed camera with a resolution of 1024x1024 and frame rate of 3000 fps. The depth of field for our optical system was estimated to be 5 mm, given by a 50 mm lens with F-number of 2.8, a nominal focus distance of 0.4 m and a camera sensor pixel size of 10 μm. Hence, given our flow domain depth of 7 mm, fine adjustment of the nominal focus distance was needed in order to be confident that the depth of field was centered on the central portion of the flow domain depth. With this depth of field only the near wall regions (ideally only 1 mm on each side of the depth of field) would not be imaged by the shadow PIV. Thus, the shadow PIV ideally represents a cross sectional average of the flow excluding the wall boundary layers.

The particles are polymer spheres (Dynoseeds®TS 40), with a density of 1050 kg/m^3 and 40 µm particle size. According to Ref. [26], tracer accuracy errors for spherical traces are below 1% if the Stokes number is significantly smaller than 0.1. Stokes number with particle Reynolds number drag correction [27] may be given by

$$St = \frac{\rho_p d_p^2 U}{18\,\mu}\psi(\mathrm{Re}_d) \tag{1}$$

where ρ_p and d_p are the particle density and diameter, respectively, and $\psi(\mathrm{Re}_d)$ is the drag correction factor. In the LVOT flow volume, the maximum flow velocity is in the order of 1.5 m/s, which by eq. (1) gives a Stokes number of $St \approx 0.005$ in our case.

The recorded shadow particle images were post processed using the open source software PIVlab [28]. The FF window deformation algorithm was used, with an interrogation window size of 32 pixels used to estimate the velocity field from the image pairs. Additionally, the velocity field is filtered by the elimination of spurious vectors from the cross-correlation signal by an outlier detection algorithm (std. threshold = 5 and epsilon = 0.15) [29], where the removed vectors are reintroduced by linear interpolation from the neighboring velocity field.

The in-plane spatial resolution for standard PIV window correlation is related to the interrogation window size [30]. However, the native resolution limit for PIV is determined by the experimental conditions where the particle image size, the particle density and the image resolution are the major contributors [31,30,32]. In our case after analysing a wide span of window correlation sizes it was concluded that a window sizes of 32x32 produced velocity estimates on our 1024x1024 pixel images that most accurately reconstructed the known prescribed inflow to the flow phantom. Hence, an estimate for the PIV resolution in our case on the 39 × 39 mm image area is a uniform Cartesian grid with cell lengths of 1.2 mm. The temporal resolution of the PIV results is governed by the time increment between image pairs which in our case is 0.3 ms.

2.3. Ultrasound vector flow imaging

Vector flow imaging (VFI) is a common term for ultrasound methods that aim to estimate the blood flow velocity vector field over time. Contrary to conventional *color-Doppler Imaging* (CDI), these methods estimate the lateral component (or components for volumetric imaging) in addition to the axial (depth) Doppler component, making display of complex blood flow dynamics possible. In this work, blood speckle tracking (BST) was used for VFI estimation, followed by a model-based regularization scheme [2,33]. BST is a method which similarly to PIV estimates displacements through image cross-correlation, but by using the blood speckle pattern inherent to the received ultrasound data as the image signature, i.e. no additional contrast agent is injected. The speckle movement is correlated to the blood scatterer movement, but only for short periods of time. A high frame rate setup in the kHz range is therefore needed for sufficient accuracy. A GE Vivid E95 ultrasound scanner (GE Vingmed, Horten, Norway) and the GE 6S pediatric transducer was used for image acquisition. A high frame rate imaging setup was implemented based on the emission of broad unfocused pulses and by beamforming several image lines in parallel for each emission. Beamformed in-phase/quadrature (IQ) data was stored to disk and processed using in-house software written in Python. The acquired IQ-data was filtered to separate the blood signal from dominating clutter signal using a 5th order high-pass infinite-response filter [34] with a cut-off frequency equivalent of 19.4 cm/s. This implies that signal from blood with an axial velocity component below this cut-off will be attenuated. This leads to dropouts in the signal as evident in Fig. 2. Blood speckle tracking was done using a combination of block matching and Doppler shift estimation, as detailed in previous work [35,33]. The kernel size used for block matching procedure was set to 1 mm^2 with a

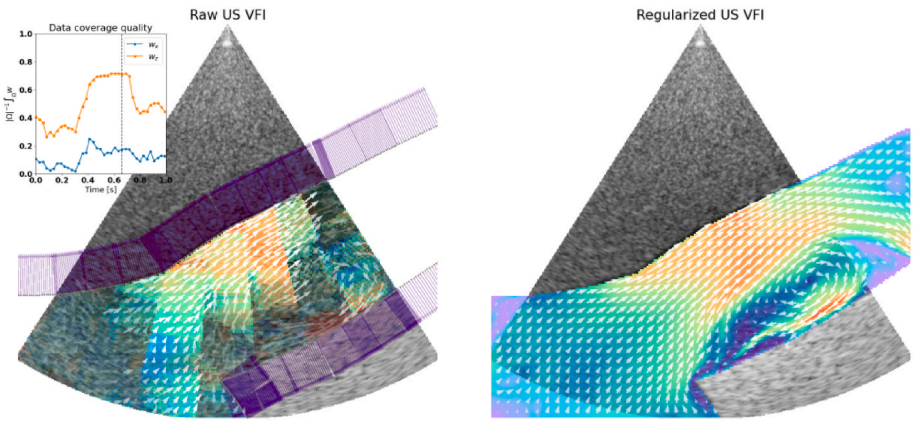

Fig. 2. Overview of the data assimilation process. The raw BST estimates are shown on the left, with tracking correlation indicated by flow opacity. Note the dropout regions produced by the wall filtering algorithm. The domain boundary and normals used in the model based regularization are drawn as purple lines. The tracking quality and domain coverage for each is shown in the top-left corner, where the tracking correlation ranging from 0 to 1 is integrated over the domain and divided by the domain area for each frame. To the right is shown the regularized flow field.

search region area equivalent to a maximum velocity of 1.0 m/s over a grid with 1 × 1 mm resolution. An overview of the parameters is found in Table 2.

The accuracy of BST is linked to the inherent image spatial resolution, which varies with depth. The lateral resolution is linked to the transmitted frequency and two-way F-number:

$$r_{lat} \approx \lambda \cdot F_{\#system} = \lambda \cdot \frac{D}{a} \tag{2}$$

where λ is the wavelength of the transmitted pulse, D is the focusing depth, and a is the effective aperture width, which for our unfocused setup is equal to the transducer footprint. For the pulse-echo axial resolution the following approximation can be used

$$r_{axial} \approx 0.5 \cdot L \tag{3}$$

where L is the spatial length of the transmitted pulse.

The aperture of the probe was estimated to be 16–18.5 mm, and we transmitted pulses of length 0.8 mm with a center frequency of 3.3 MHz. Unfocused transmit pulses were emitted, and dynamic focusing was applied during receive beamforming. The flow region of interest was at depths of 5–8 cm, where we approximate the resolution to be within the range of $r_{lat} = [1.3, 2.3]$ mm, with an axial resolution of about $r_{axial} = 0.40$ mm.

For the temporal resolution two different time scales are relevant; the estimation rate and the frame rate. Due to an interleaved (duplex) acquisition of B-mode (anatomy) and blood speckle frames, an ensemble ($N = 12$) of transmissions are acquired at the high frame rate (kHz range) which are processed to one velocity estimate for each pixel. The estimation rate is set by the pulse repetition frequency, $PRF = 5000$ Hz, resulting in a temporal resolution of $\delta t_{est} = 0.2$ ms. The measurement frame rate depends on the width and depth of the scan, the size of the flow region of interest, and B-mode parameters. In our setup this was about 36Hz, corresponding to a temporal resolution $\delta t_{frame} = 28$ ms.

Table 1
Summary of solution space, solver and model parameters.

Parameter	Value
Grid axes	[t, x, z]
control points	[128, 256, 256]
order	[3,1,3,1]
periodic	[Yes, No, No]
Variables	[v_x, v_z, ρ]
Learning rate	1e-3
c	1024 m/s
ρ_0	1e3 kg/m^3
λ	0.05
Iterations	1000

Table 2
The setup of the three methods; US, PIV and CFD, are summarized in the table.

	US	PIV	CFD
Raw data basis			
Type	Doppler velocity field Speckle images	Optical images	Numerical grid
Spatial resolution [mm]	0.40(axial), 1.3–2.3 (lateral)	0.038	0.15–0.5
Frame rate [Hz]	36	3000	20000
Shutter type	rolling (28 ms)	global	
Raw velocity estimation			
Estimation method	Doppler(axial) + lateral block matching	Block matching	
Estimation rate [Hz]	5000	3000	
Kernel size [mm^2]	1.0	1.44	
Sample spacing [mm]	1.0	0.3	
V_{res} [m/s]	0.1		
V_{max} [m/s]	1.5		
Post processing			
Regularization method	Model based b-spline fitting	Outlier detection [29] Linear re-interpolation	
Comparison output grid			
Size	128x128 pixels		
Extents	39x39 mm		
Spatial resolution	0.3 mm		
Temporal resolution	1 ms		

To deal with measurement variance and dropouts due to the clutter filter during parts of the cardiac cycle, smoothing of the measured vector field is required. Gaussian smoothing is efficient in reducing variance, but significant amounts of detail is lost in the process. The BST estimation was therefore subsequently post-processed using our in-house regularization framework *TensorSpline*. Variational data assimilation was done towards a latent variable model based on the weakly compressible Euler equations, aiming to smooth the flow in a physically consistent manner. The assimilation procedure uses a triquadratic B-spline basis to compute the data fit, which is balanced towards model deviation during the optimization of the B-spline control points. The variational problem is solved with the TensorFlow framework through error-backpropagation using automatic differentiation of a cost function comprised of terms describing both fitting errors and deviation from the model integrated numerically over the domain. Let θ be a coordinate in the vector function space spanned by the tensor product B-spline basis with each control point containing the vector components [v_x, v_z, ρ], then the cost function

$$\mathcal{J}(\theta) = \frac{\widehat{T}}{\widehat{L}} \underbrace{\sum_i \mathbf{w}_i \left\| \mathbf{v}^*(\mathbf{x}_i) - \alpha \mathbf{v}_i \right\|}_{\text{Data fitting}} + \frac{\widehat{T}}{\widehat{L}} \underbrace{\sum_i |\mathbf{v}^*(\mathbf{x}_i^{\text{wall}}) \cdot \widehat{\mathbf{n}}^{\text{wall}}|}_{\text{Free-slip condition}} \tag{4}$$

$$+\lambda \left[\frac{\widehat{T}^2}{\widehat{L}\rho_0} \underbrace{\int_\Omega \left\| \frac{D\mathbf{v}^*}{Dt} + c^2 \nabla \rho^* \right\|}_{\text{Momentum continuity}} + \frac{\widehat{T}}{\rho_0} \underbrace{\int_\Omega \left| \frac{D\rho^*}{Dt} + \rho^* \nabla \cdot \mathbf{v}^* \right|}_{\text{Mass continuity}} \right] \tag{5}$$

solves the fluid assimilation problem, where $\mathbf{v}^*(\mathbf{x}) = [v_x^*(\mathbf{x}), v_z^*(\mathbf{x})]$ and $\rho^*(\mathbf{x})$ represents evaluating the velocity and density solution variables at a location $\mathbf{x} = [t, x, z]$ in the domain given the control points θ. In the integral terms the position is omitted for compactness and should be understood as evaluation over the integration measure. The integrals are computed numerically over the assimilation domain Ω using Monte-Carlo integration. The input data $(\mathbf{x} = [t, x, z], \mathbf{v} = [v_x, v_z], \mathbf{w} = [w_x, w_z])_i$ contains the position, velocity and uncertainty measure of each vector velocity estimates obtained from the BST procedure and the wall data $(\mathbf{x}^{\text{wall}} = [t, x, z], \widehat{\mathbf{n}}^{\text{wall}} = [\widehat{n}_x, \widehat{n}_z])_i$ contains the boundary position and normals. $\widehat{T}$ and $\widehat{L}$ is the temporal and spatial domain extent respectively, ρ_0 is the rest density of the fluid and c^2 is the incompressibility coefficient roughly related to the speed of sound in the fluid. $\alpha = \Sigma_i w_i \|\mathbf{v}_i\| / \Sigma_i w_i \|\mathbf{v}^*(\mathbf{x}_i)\|$ is an adaptive magnitude gaining term added to offset the underestimation introduced by the regularizing parameter $\lambda > 0$. The solution tensor

$$\theta^* = \arg\min_\theta \mathcal{J}(\theta) \tag{6}$$

is found through adaptive gradient descent using the Adam optimizer. A spatial B-spline sampling grid of 256 × 256 control points in the lateral and axial directions, and a periodic temporal interpolation window of 128 control points was used. The regularization method parameters was tuned to provide a smooth flow field while limiting underestimation, an inherent trade-off. An uncertainty measure of BST quality based on the correlation magnitude was used to balance trust in the measured data versus the model. The hyperparameters used in the assimilation process is given in Table 1.

2.4. CFD model

The PIV and US obtained their raw data from measurements on the actual geometry. In order to perform a CFD simulation of the experiments one needs a set of consistent boundary conditions (BC's), initial conditions (IC's) and an accurate representation of the geometry. In theory one could simply rely on the underlying CAD used to produce the different parts of the flow rig, and the data used to control the linear actuator which produces the pulsating flow in the rig. However, as trained practitioners will know, manufacturing often introduces subtle simplifications and changes that are either not communicated, or which result from assembly. Thus, we adopt an empirical approach to defining the geometry, IC's and BC's for the CFD-problem. First we supplement the original CAD drawings with measurements made on the actual geometry when it is mounted in the flow rig. Next, we visually observe the flow field in the experimental flow loop and define the extent of the computational domain needed to give robust boundary conditions. PIV measurements were made of the actual inlet flow rate conditions to this domain, and a uniform velocity profile based on the estimated PIV flow rate was used as an inlet profile to the CFD domain. The pressure outlet was located at a downstream position where a relatively uniform flow had developed. This procedure improved the correspondence between the CFD predictions and the PIV measurements in the LVOT-region substantially. Since we were unable to obtain PIV measurements of the entire computational domain it was not possible to obtain initial conditions (IC's) for the entire domain. To remedy this we would run the simulation for eight consecutive cycles and use data from the last four cycles in our analysis. The Reynolds number of the flow peaks at about 6000, but the pumping action only last for about 250 ms. Thus, there is little time to develop a fully turbulent flow and boundary layers. Boundary layer thickness at peek systole will be of the order $\delta \approx \sqrt{\nu t}$. Substituting $\nu = 1.0 \cdot 10^{-6}$, and $t \approx 125$ ms we get $\delta \approx 350$ μm as a maximum boundary layer thickness. The Womersley number for the flow is, using 30 mm as length scale (large aorta root diameter), water at density of 1000 kg/m^3, viscosity at room temperature of 1 mPa· s/cPoise and a pulse rate of 60 beats per minute, $\alpha \approx 37.6$ (for blood this value would be $\alpha \approx 20$ for 60 BPM and ≈ 18 for 72 BPM. This means that transient inertial forces dominate over viscous forces, resulting in a flat velocity profile. Based on the Womersley number the boundary layer thickness is estimated at 0.4 mm for this experimental set-up. This is consistent with the simple estimate using boundary layer theory for a flat plate given above.

The flow was solved using ANSYS Fluent 19.2. The transient, incompressible, pressure based solver was used. Different turbulence models were investigated. We found that there was little difference between results obtained using the laminar model and three different different turbulence models. The models investigated were: $k-kl-\omega$, LES with the WMLES S-ω sub-gridscale model, DES with SST $k-\omega$ RANS model and the DDES shielding function. Since the flow is time periodic on a time scale of $1/HR$ we do not believe statistical turbulence has time to form during systoli and we elect to use a laminar flow model. This also removes complications in justifying selection of model constants needed in the different turbulence models. It should also be noted that in reality blood is a fluid containing formed elements such as red blood cells that are of the order 6–10 μm, and white blood cells 14–16 μm.

We used the SIMPLE scheme for the pressure-velocity coupling, spatial discretizations were done using a second order and second order upwind schemes. The time discretization was first order implicit. For the DES simulation a bounded second order implicit transient formulation was used. The computational grid (x1) consisted of roughly 790k hexahedral control volumes. Wall boundary layers consisted of a starting cell size of 150 μm growing geometrically by a factor of 1.12–500 μm. A fixed time-step of 50 μs was used.

The resolution of the computational grid was determined from a grid sensitivity analysis of three test grids: x0, x1(as described above) and x2. Grid ×0 had a maximum grid cell size of 1200 μm and was chosen to coincide with the resolution in the PIV system. The resolution of grid ×2 was double that of grid x1, i.e. 75-250 μm. An illustration of the results found in the grid sensitivity analysis can be seen in Fig. 3, where velocity y-components are plotted at the aortic root at time points t_1 and t_3.

2.5. Flow field resolution comparison

In this work we have compared three methods; US, PIV and CFD for obtaining flow field information for a physiological relevant geometry, an in-vitro model of the human LVOT. The temporal and spatial resolution in our case for the three methods are different which is of significance when interpreting the results. In order to compare the results, we have interpolated (linearly) the results from the three methods onto a 128x128 grid with a time step of 1 ms. The 128x128 grid is bounded to the PIV measurement area defined in Fig. 4b, which measures 39 × 39mm and therefore produces a spatial resolution of 0.3 mm/grid cell. The native spatial and temporal resolution of the three acquisition methods (US, PIV and CFD) are given in the three previous sections, and summarized in Table 2.

2.6. Flow field analysis

In this section we provide some mathematical measures for describing a flow field which will be used in the analysis of the results and the comparison between US, PIV and CFD. A general flow field may be represented by the Eulerian velocity field

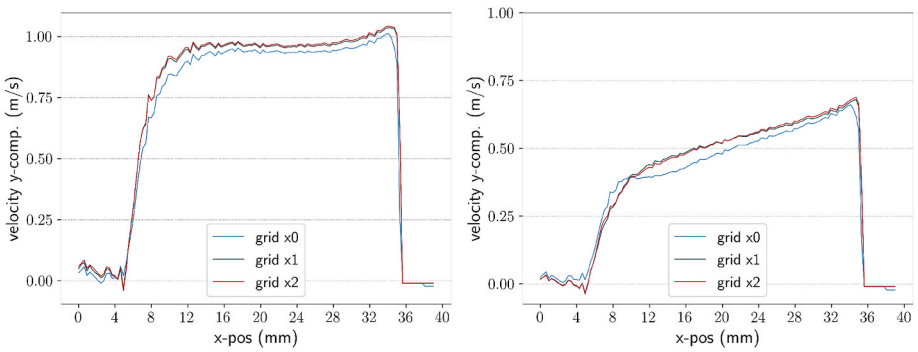

(a) Time point t_1 (b) Time point t_3

Fig. 3. CFD grid sensitivity analysis. Velocity y-components plotted at the aortic root at time points t_1 and t_3.

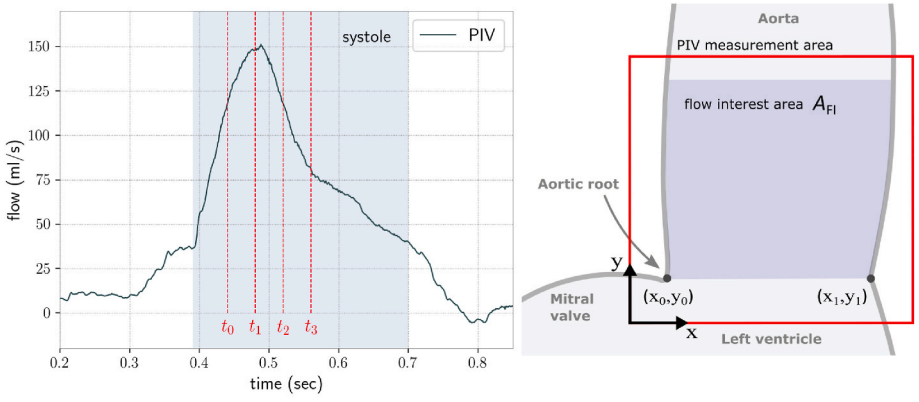

(a) Flow rate curve and time points (b) LVOT flow field layout

Fig. 4. a) Volume flow curve from PIV. Showing the systolic time range, and time points of interest for the following data analysis t_0, t_1 and t_2. b) Illustration of layout of the flow field in the LVOT captured by the three modalities US, PIV and CFD. The PIV area imaged by the high speed camera is indicated by the red rectangle (see also Fig. 1). The "flow interest area" is defined by the blue colored region, and the following data comparison between the three modalities will be concentrated within this area. A coordinate system position is chosen where the origin is placed at the notch of the aortic root connecting the LVOT and the mitral valve.

$$\mathbf{v}(\mathbf{x},t) = v_i(\mathbf{x},t), \quad i = \{x,y,z\} \tag{7}$$

where $\mathbf{x}$ is the position vector and t is time. The spatial gradient of the flow is given by the velocity gradient

$$\boldsymbol{l} = \nabla \mathbf{v}^T = l_{ij}. \tag{8}$$

The velocity fields in this work will have vortexes and regions of back-flow. A vortex core may be defined as connected regions of pressure iso-surfaces around a pressure minimum (although pressure minimums can occur without the presence of a vortex). The geometry of such vortex cores can be described by the λ_2-criterion, presented by Ref. [36], which is derived from considering the spatial gradient of the Navier-Stokes equations. The spatial gradient of the incompressible Navier-Stokes equation may be presented as

$$\frac{Dl_{ij}}{Dt} + l_{kj}l_{ik} - \nu\nabla^2 l_{ij} = -\frac{1}{\rho}p_{,ij}, \tag{9}$$

where $p_{,ij}$ is the pressure Hessian; and ρ and ν are density and kinematic viscosity, respectively. The λ_2 criterion is defined by the eigenvalues λ_1, λ_2 and λ_3 of the symmetric decomposition of the second term in eq. (9), i.e. $\frac{1}{2}(l_{kj}l_{ik} + l_{jk}l_{ki})$, hence neglecting the unsteady straining and viscous effects. A vortex core is then defined as regions where $\lambda_2 < 0$ (for an in-depth derivation see e.g. Refs. [37,36]).

In the following we will also also examine the curl of the velocity field, given by

$$\mathbf{w} = \nabla \times \mathbf{v}. \tag{10}$$

3. Results

3.1. vol flow, peak velocity and kinetic energy

The volumetric flow rate $q(t)$ is calculated for the three modalities (US, PIV and CFD) by integration of the velocity field over a plane spanning the aortic rot, from x_0 to x_1 as given in Fig. 4. Hence, the volumetric flow is given by

$$q(t) = h\int_{x_0}^{x_1} v_y(x,t)\,dx, \tag{11}$$

where, h is the channel depth. Another measure of interest is the maximum velocity recorded by the three modalities US, PIV and CFD during the cardiac cycle

$$V(t)_{\max} = \max_{\mathbf{x}\in A_{FI}} V(\mathbf{x},t) \tag{12}$$

where $V(\mathbf{x}, t)$ is the velocity magnitude, and where the maximum value is given by the 99% percentile.

The results from the volumetric flow rate analysis can be seen in Fig. 5. From Fig. 5 one can observe that the flow rate for the three modalities US, PIV and CFD follow each other closely for the majority of the systolic period except during diastole, where US slightly underestimates the flow rate through the Aorta. The maximum flow velocity in the LVOT is similar for PIV and CFD, while US underestimates the velocity magnitude by approximately 17%, respectively during systole. As seen in Fig. 5-b.

The kinetic energy of a unit of moving fluid with mass m and velocity v is

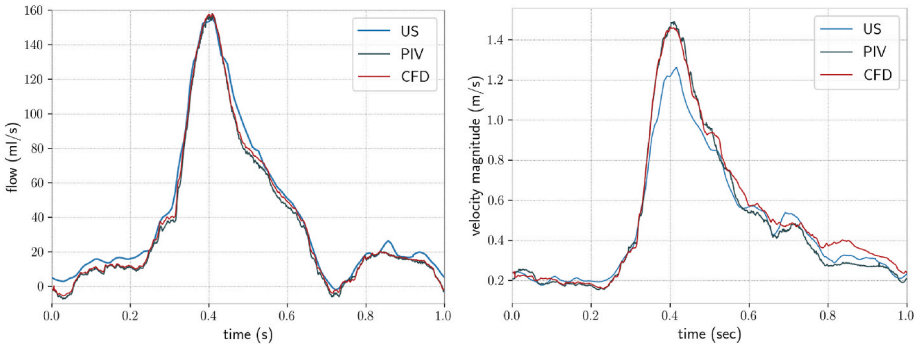

(a) Flow rate curves (b) Maximum velocity magnitude

Fig. 5. a) Volumetric flow rate $q(t)$ for the three modalities US, PIV and CFD as given by eq. (11). b) Maximum velocity magnitude $V(t)_{\max}$ for the three modalities US, PIV and CFD as given by eq. (12).

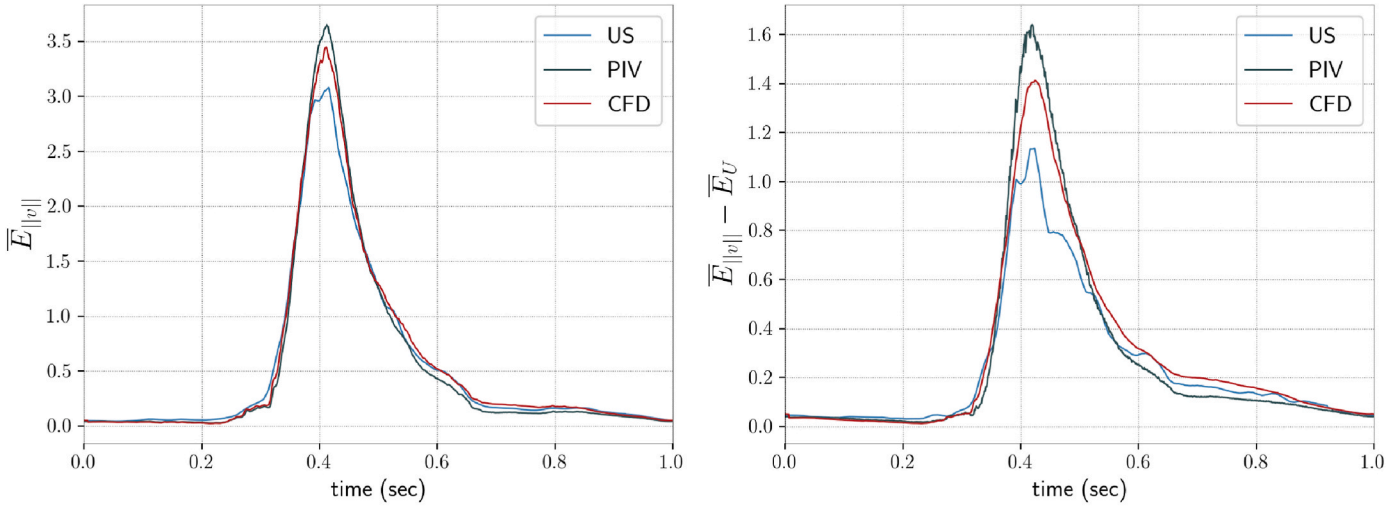

(a) total kinetic energy

(b) excess kinetic energy

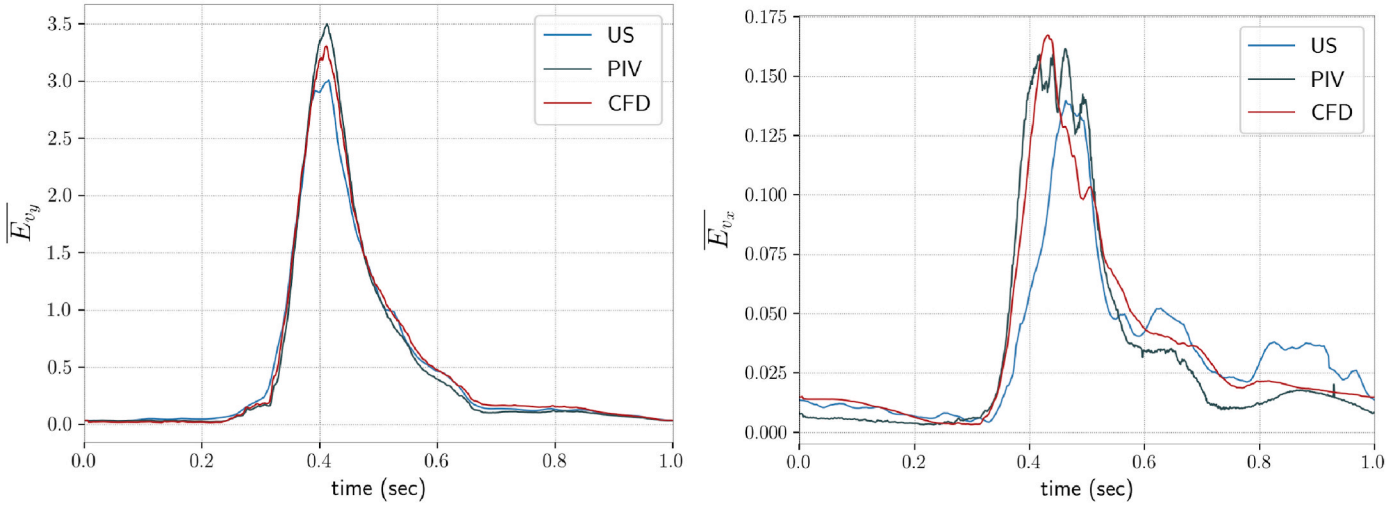

(c) kinetic energy y-direction

(d) kinetic energy x-direction

Fig. 6. a) Total weighted kinetic energy, for the three modalities US, PIV and CFD b) Weighted kinetic energy (solid lines) and kinetic energy given plug profile (dashed lines), in the axial direction. c) Weighted kinetic energy in transverse direction.

$$E = E_k = \frac{1}{2}mv^2 \tag{13}$$

For a flow field region with area A_{FI}, the area weighted kinetic energy of the fluid in that region at a given time can be calculated by

$$\bar{E} = \frac{1}{A_{\mathrm{FI}}}\int_{A_{\mathrm{FI}}} \frac{1}{2}mv^2\, dA \tag{14}$$

The area weighted kinetic energy in the transverse and axial directions can be investigate by substituting in the velocity components in the x and y directions, respectively. Likewise the total kinetic energy is given by the velocity magnitude $\|v\|$. Furthermore, we will also calculate the kinetic energy based on the unidirectional superficial flow velocity $U = q/A$, to compare the kinetic energy difference, given by $\bar{E}_{\|v\|} - \bar{E}_U$, between our case where vortexes and back flow develop during the cardiac cycle and a unidirectional plug flow scenario.

From Fig. 6 it is clear that the axial direction (y) is dominant with regards to the kinetic energy of the flow. Additionally, there are some differences between kinetic energy components of the US flow compared to PIV and CFD data especially in the transverse direction. In Fig. 6b, one can also quantify the energy loss created by eddies with regions of back flow induced by the phatological geometry of the LVOT and the distortion of the velocity profile due to viscous forces. This can be done by comparing the kinetic energy of the flow under the assumption of a plug flow profile (i.e. flat velocity profile due to no loss) to the weighted kinetic energy in the flow region of interest. And, as can be computed from Fig. 6a and b, at peek systole, the energy loss in the flow region of interest compared to a plug flow profile is approximately 37% for US, 45% for PIV and 40% for CFD. The vorticity of the flow field is of interest as a means to characterize the flow and the differences between the three modalities US, PIV and CFD. The major rotational structures are expected to be in the xy-plane hence from eq. (10) the curl component

$$w_z = \frac{\partial v_y}{\partial x} + \frac{\partial v_x}{\partial y} \tag{15}$$

is investigated. The intensity of the rotational components of the flow can be quantified by calculating the maximum value of the curl in A_{IF} during the cardiac cycle, hence we define

$$w_{z,\max}(t) = \max_{\mathbf{x}\in A_{\mathrm{FI}}} w_z(\mathbf{x}, t) \tag{16}$$

where the maximum value is given by the 99% percentile. The maximum curl intensity during the cardiac cycle is given in Fig. 7, and is of similar magnitude for PIV and CFD during the cardiac cycle. When comparing the curl magnitude from US to PIV and CFD, it is clear that the rotational motion of the flow starts later in the cardiac cycle in the US results, and that the curl intensity magnitude is significantly lower during systole.

REMARK FOR REVIEW: Compared to the original version of the paper, Fig. 9 now shows contours of the λ_2-criterion in without any normalization and low pass filtering. Hence, the visualization now includes low contour values showing features which were suppressed in the original version of the paper.

3.2. Velocity profiles

Normalized velocity profiles for US, PIV and CFD at three locations in the flow area of interest are given in Fig. 8. The profiles are colored by the velocity component in the y-direction (axial direction) at time-points t_0, t_1, t_2 and t_3 as defined in Fig. 4. From Fig. 8 it is clear that the profiles for PIV and CFD are similar in shape and magnitude especially for time points t_0, t_1 and t_2. The profiles from US follows the overall shape and magnitude of PIV and CFD, however the US profiles are more rounded compared to PIV and CFD (the transition from low to high velocity zones in the transverse cross section is sharper for PIV and CFD).

3.3. Vortex structure of the flow field

The vortex structure in the LVOT for US, PIV and CFD at time points t_0, t_1, t_2 and t_4 are given in Fig. 9. In our case, with a mitral valve which is to some extent bulging into the atrium, the flow into the aorta is dominated by a strong vortex which is generated at the start of systole at the sharp angle between the mitral valve leaflet and the aortic root. The lower panels in Fig. 9 illustrates regions of back flow (i.e. flow in the negative y direction) visualized with a yellow contour area along with vortex structures visualized by black contour lines given by the λ_2-criterion. Two main features that distinguishes the vortex field observed in PIV to US and CFD can be identified; 1) for US, the dominant vortex propagates further into the domain (in the positive x-direction) when compared to PIV and CFD, and the main vortex in the US data is generated further from the aortic root (in the positive y-direction) at the start of systole compared to the PIV and CFD data; 2) for CFD the main vortex structure is composed of several smaller vortexs and not a single smoothed structure as seen in the cases for US and PIV. These two observations can be further studied in Fig. 10, where the dominant vortex position in the flow field have been tracked over time from contours given by the λ_2-criterion. Here one can also observe that the rotational center of the main vortex structure for CFD, as given by the λ_2 criterion, is less regularly defined during its propagation through the LVOT during systole compared to US and PIV, which is caused by the fact that the main vortex for CFD is composed of several smaller vortexes.

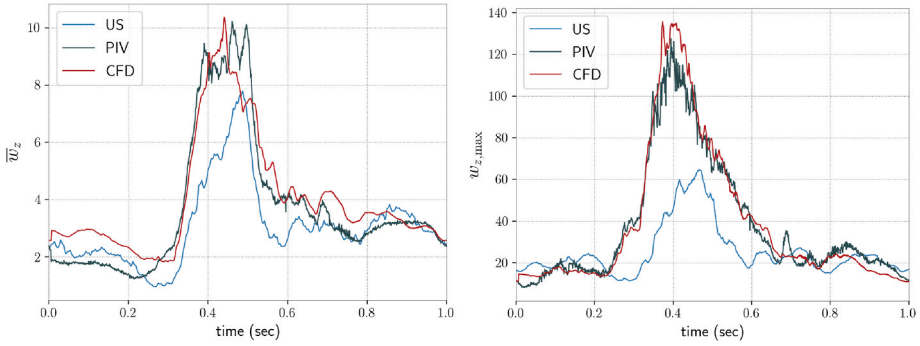

(a) Mean curl intensity (b) Maximum curl intensity

Fig. 7. a) Mean $\bar{w}_z$ and b) maximum curl intensity $w_{z,\max}$ during the cardiac cycle, for the three modalities US, PIV and CFD.

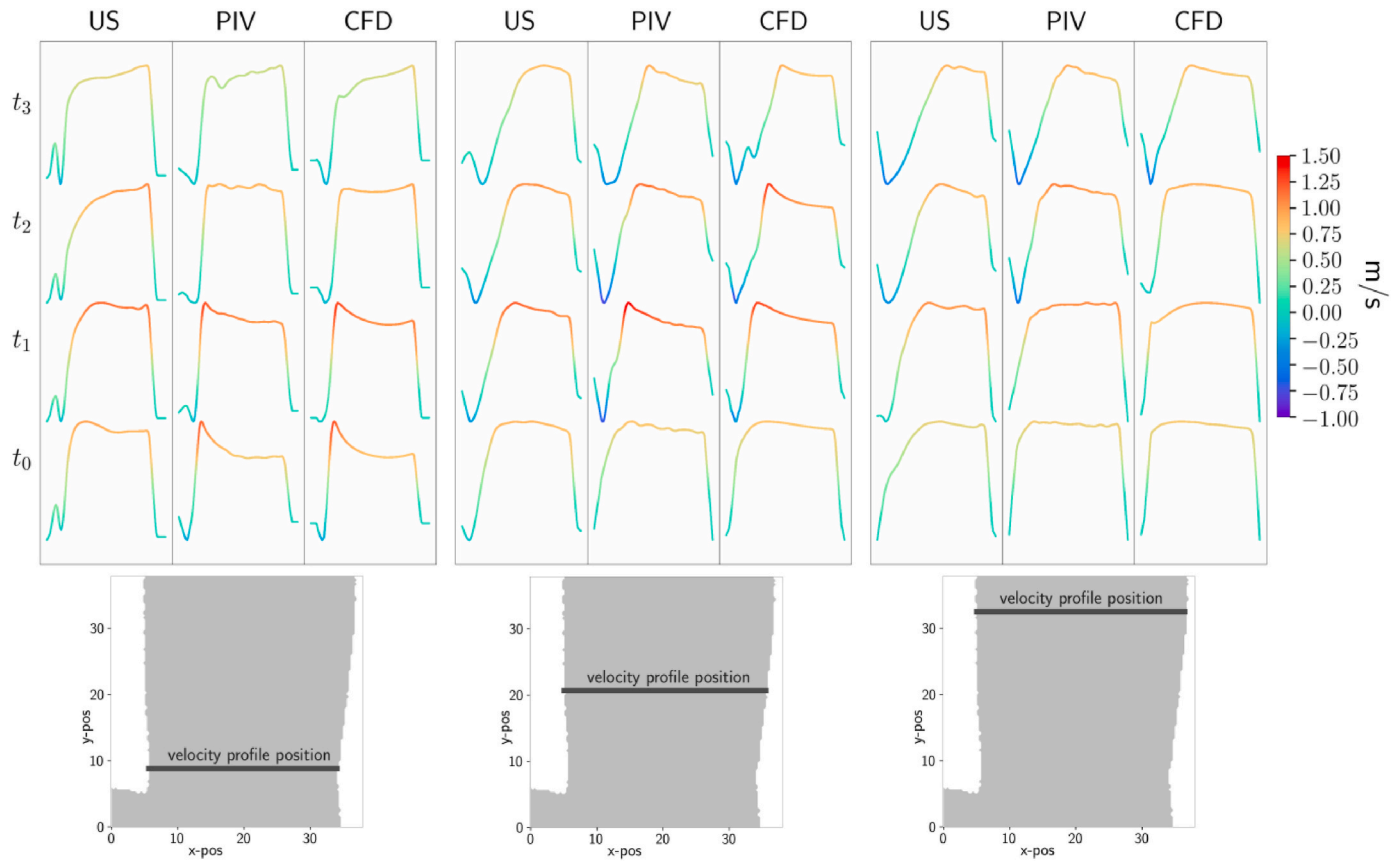

Fig. 8. *Top panels*: Normalized velocity profiles for US, PIV and CFD at three locations, colored by the velocity component in the *y*-direction (axial direction) at time-points t_0, t_1, t_2 and t_3 as defined in Fig. 4. *Bottom panels*: Velocity profile position in the *y*-direction (axial direction) for the three top panels.

3.4. Flow field regularization

The velocity field given by ultrasound BST have in this work been model regularized by the compressible Euler equations (see Sec 2.3). The aim of the model regularization is to enable more choerent estimates and smoothing of the two-component flow field. The level of smoothing introduced by the regularization is investigated by comparing the PIV data to regularized PIV, i.e. the PIV data set has been regularized by the regularization scheme used on the US data. The results can be seen in Figs. 11 and 12, where the PIV data is given alongside regularized PIV. From Fig. 11a, it is clear that the regularization produces an sligth underestimated volumetric flow rate when compared to the PIV results, which is on the order of 10% lower at peak systole. The underestimation of the flow field is caused by a smoothing of the velocity components, which is visualized in Fig. 12 where contours of velocity magnitude is given for the PIV data is given alongside regularized PIV at time-points t_0, t_1, t_2 and t_3. The figures show that the regularization reduces spatial velocity gradients and peak velocities.

4. Discussion

In this work two measurements techniques US and PIV and one purely numerical method, CFD, have been used to obtain detailed 2D velocity vector fields of a pathological model of the LVOT. The flow field produced is not a simple rectilinear flow profile but comprises of complex vortical structures that migrate both temporarily and spatially. Capturing and characterizing such complex flow phenomena is challenging for all three "flow characterization modalities" US, PIV and CFD. For US and PIV, the measurements were obtained in synchronized laboratory experiments from a combined optical and ultrasound compatible flow phantom. Subsequently, a CFD model of the lab setup was created and numerical simulation of the model setup was carried out using flow boundary conditions obtained from the PIV measurement data. Our approach therefore makes it possible to make direct comparison of the flow fields obtained using the different techniques PIV, VFI and CFD.

4.1. Flow field comparison between modalities

The results of the laboratory experiments from US and PIV and the numerical results from the CFD model have in the previous chapter been compared with regards to: integrated flow rate; maximum velocity magnitude; velocity profiles; vortex structure, maximum curl intensity; and kinetic energy.

The comparison of the flow rate at the aortic root (Fig. 5-a) and the maximum velocity magnitude (Fig. 5-b) shows that US in this case predicts the correct flow rates but under estimates the maximum velocity magnitude during peak systole. The two identified factors that contribute to the under estimation of the velocity components are; the regularization of US flow field; and US aliasing. The US regularization introduces some smoothing of the velocity components as shown in Figs. 11 and 12, where PIV and regularized PIV are compared which resulted in a 10% underestimation of the flow rate of the regularized PIV. From this result it is reasonable to assume that a similar quantity of underestimation contributes in the underestimation of the maximum velocity magnitude for the US results compared to the PIV (which is 20% in our case), hence introduced by smoothing from US regularization.

Velocity profiles at three locations in the LVOT and four time points during systole is given in Fig. 8, by the axial flow component (v_y). The velocity profiles from the US in the current work, compares reasonably well with the PIV and CFD profiles, however the velocity gradients in the transverse direction (*x*-direction) are less sharp for the US case. This we

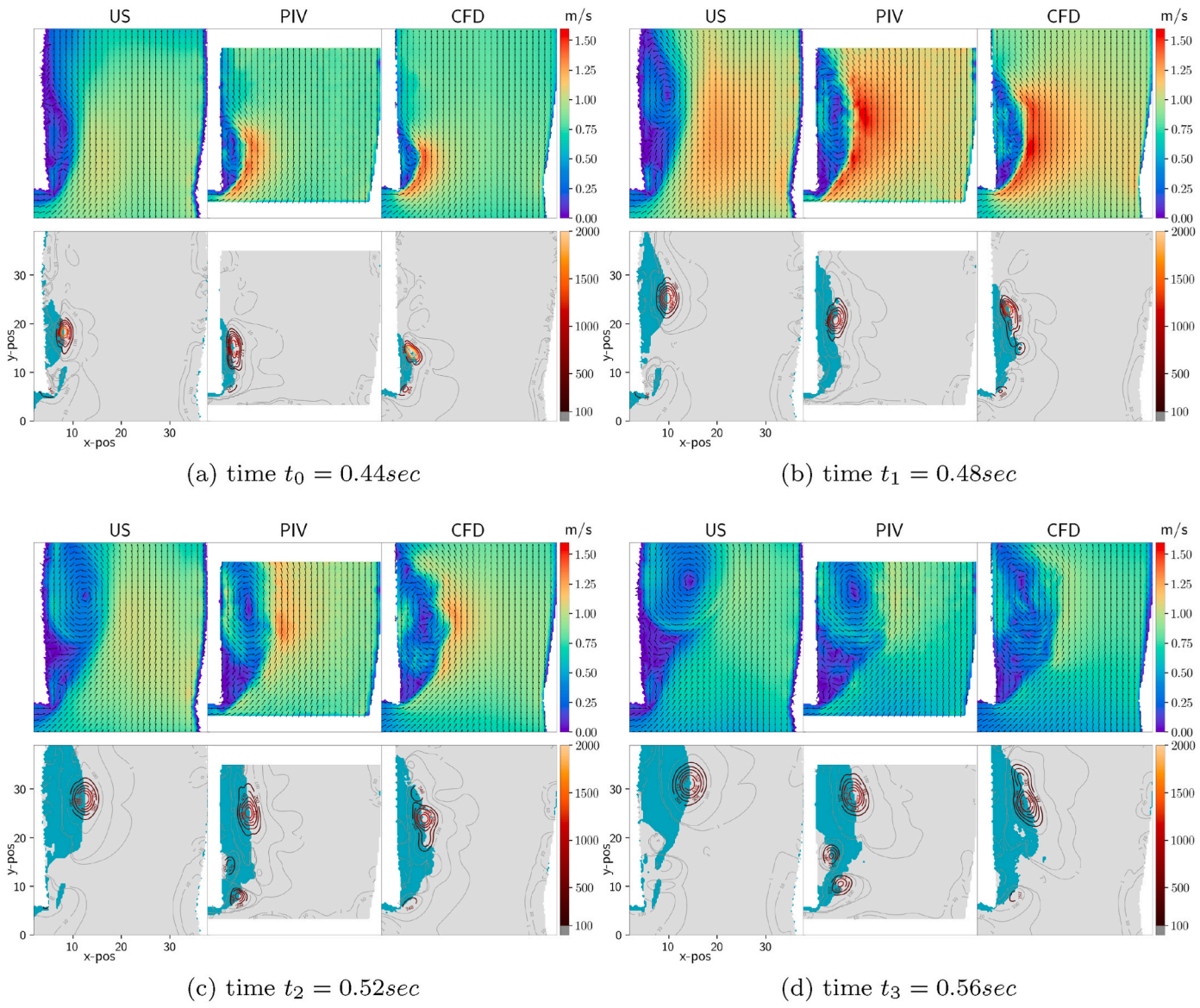

Fig. 9. *Upper panels*: Velocity magnitude contours and vectors. *Lower panels*: regions of back flow (cyan regions) and contours lines from the λ_2-criterion (unit: $\frac{1}{sec^2} \times 100$). λ_2-criterion contour lines with values less than 10000/sec^2 are colored grey to enhance the major vortex structures, which are colored with a dark-red to orange color map.

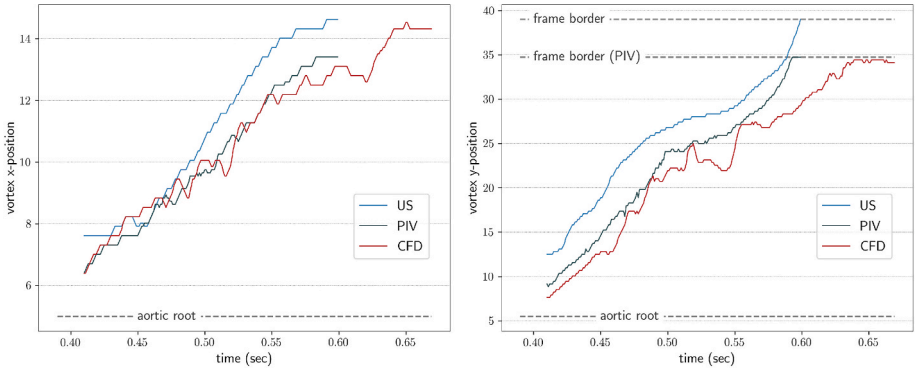

Fig. 10. *Left panel*: Dominant vortex *x*-position (mm). *Right panel*: Dominant vortex *y*-position (mm).

attribute to the smoothing effect of the US regularization and the lower spatial resolution in the US data basis compared to the two other methods (see Table 2). Generally there is good agreement between the CFD and PIV profiles. To a large extent this may be attributed to the quality of the boundary conditions for CFD model which was derived from the experimental setup, i.e. the inflow boundary condition is

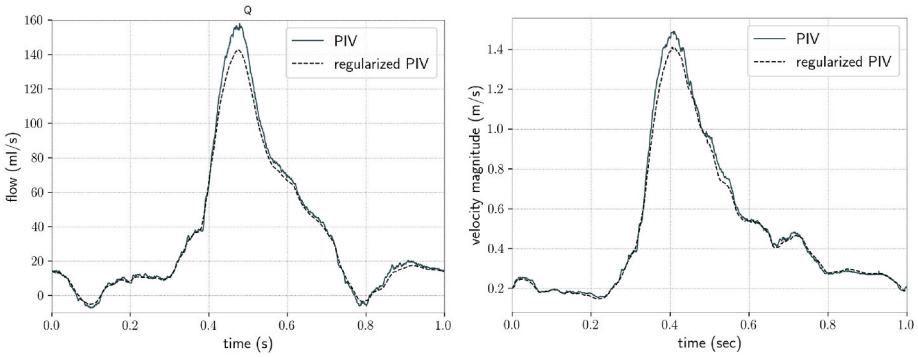

(a) Flow rate curves (b) Maximum velocity magnitude

Fig. 11. a Volumetric flow rate $q(t)$ for PIV and regularized PIV given by eq. (11). b) Maximum velocity magnitude $V(t)_{\max}$ for PIV and regularized PIV as given by eq. (12).

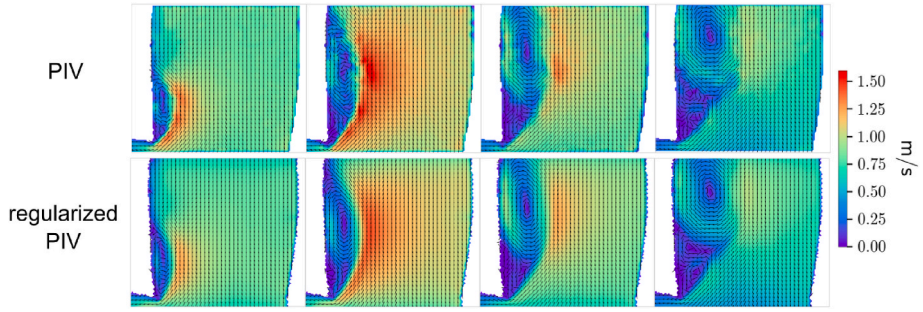

Fig. 12. Flow field comparison between PIV (upper panels) and regularized PIV (lower panels) given velocity magnitude contours and vectors, at time-points t_0, t_1, t_2 and t_3 as defined in Fig. 4.

prescribed from the flow rate measured with PIV and the geometry of the flow domain is measured directly flow the experiential setup (as outlined in section 2.4). This level of boundary condition quality is unattainable in the in-vivo setting with the current available imaging techniques, e.g. US, Doppler US and MRI. Hence, a possibly next step from our work is to compare the performance of a CFD model in a controlled in-vitro setting with boundary conditions from the experimental setup with a CFD model with boundary conditions (domain geometry and flow) from an in-vivo capable imaging technique such as regularized US.

The narrowing of the flow channel, i.e., following the path of the mitral valve plane, around the aortic root and into the ascending aorta (see Fig. 4b) combined with the sharp angle of this contraction (over 90°), will at even modest flow rates cause boundary layer separation and the creation of a region of back flow/wake and vortex generation. Generally, a wake is formed from the detachment of a boundary layer resulting in flow separation. This phenomenon occurs when the flow is slowing down, i.e., flowing in an adverse pressure gradient, for example after an acceleration caused by a narrowing of the flow channel [38]. If the flow slows down enough to stop and reverse direction relative to the solid boundary a wake is formed and the flow detaches and forms eddies and vortices, which is the phenomena observed in our case downstream of the aortic root notch at the ascending aortic wall. The generation and migration of a vortex is not a fully predictable phenomenon especially for dynamic inflow conditions. Additionally, in our case the frequency of the inflow pulses does not allow the flow field to settle to rest before the next flow pulse is initiated. Thus, a residual curl is part of the flow at the inception of the systole. However, in our case there is little change in this residual curl from pulse to pulse making the flow mainly time-periodic, and all three modalities were able to capture this residual curl (Fig. 7). In our system, the main feature of the vortex structure is a large vortex which is initiated at the aortic root at the start of systole and which propagates downstream of the LVOT during systole (Fig. 9). The migration track (Fig. 10) and size of this dominant vortex compares well between US and PIV, which is reasonable because the US and PIV were synchronized during the lab measurements and recorded the same vortex. The major features of the vortex structure during systole also compares well between the CFD results and US and PIV. In the CFD case, the main vortex occasionally have more than one rotation center during systole which is consistent with the variability observed in the flow experiments between flow pulses. This variability is attributed to the fact that vortex creation, stability and interaction to some extent is a stochastic process, hence, although the main structure of the vortex field should be the same between heart beats some differences on the more detailed level is expected. However, the CFD case predicts the correct level of curl maximum intensity in the flow domain compared to PIV as seen in Fig. 7. A significant difference in the curl magnitude can be found when comparing US to PIV and CFD. For US the rotational component of the flow seams to be delayed at the start of systole compared to PIV and CFD and the curl intensity magnitude is lower throughout systole. To a large extent, these artifacts can be attributed to the smoothing effect of the US regularization which lead to less steep velocity gradients, which can be observed in the velocity profile plots in Fig. 8, when comparing the change in velocity when moving toward the solid boundaries between US and PIV, and CFD. Another observed difference when comparing US with PIV and CFD is the migration path of the main vortex during systole in the LVOT. At the start of systole a vortex is generated at the aortic root. This vortex propagates into and downstream the LVOT. The flow path of this vortex is in the downstream direction (y-direction) is in essence the same between the three modalities, as can be seen in Fig. 10. In the transverse direction (x-direction) however, the US vortex is generated futher from the aortic root and propagates too far into the domain, when compared to PIV and CFD. We speculate that this may be caused by an improper weight balance between the velocity components

in the direction of and transverse of the US beam after regularization of the US data.

4.2. Vector flow imaging

Blood flow measurements using ultrasound are prone to several limitations, where resolution, signal-to-noise ratio (SNR), and clutter influence are important factors. In an in-vivo scenario it is hard to adapt the clutter filter to local variations within in the imaging region over time. It can either cause underestimation of velocities where clutter from the surrounding tissue is not sufficiently rejected, or signal drop-outs where the Doppler frequency of the blood is lower than the filter cut-off. In this experimental in-vitro setup we have minimal influence from the surrounding tissue after the applied filter, due to the low velocities in the tissue mimicking PVA. However, since we are using a filter adapted for a realistic scenario, we will get regions of signal drop-out, where we have no confidence in the raw velocity estimates.

The SNR in this setup can be considered relatively high, due to the acoustic window into the imaging region, in contrast to an in-vivo scenario where ribs and lungs can have significant negative impact on the image quality. We could, however, get destructive contributions coming from strong reflections from the Plexiglas plates on both sides of the 2d flow plane, due to misalignment's with the UL transducer. This could cause decorrelation in the processed blood speckle signal, and hence an increased variance in the estimates. Placement of the probe was aimed to reduce this effect to a minimum, but only by eye-balling the image quality during alignment.

The difference in resolution, as approximated in section 2.3, in addition to the phase-information we have in the axial direction, gives us better performance when estimating velocities in the axial direction relative to the lateral. Due to this difference, the orientation of the main flow direction affects the estimation performance. In this scenario, we obtained a view in between a clinical long axis and short axis, where the lateral components constitute a large part in the overall flow vector field. Hence, it could be expected that a view that was more aligned with the LVOT direction would have resulted in better performance and vice versa. While the frame rate of which the velocity estimates was acquired was 5 kHz, by using packet acquisition, the resulting temporal frame rate of the resulting BST frames was 27 ms (~37 Hz).

4.3. Experimental setup and shadow PIV

The experimental setup for the flow loop was designed to allow for synchronized shadow PIV and US measurements, and to produce a predominantly 2D flow field at the center section of the LVOT. For the shadow PIV flow velocity measurement technique it is favorable for one of the axis of the flow domain to be relatively thin to allow advocate illumination by back-light through a particle dense field. However, other experimental options could be exploded, i.e. a deeper flow field and less dense particle field and particle plane selection based on out of focus rejection. The shadow PIV technique have some noticeable drawbacks compared to laser sheet PIV, i) The minimum particle size and ii) flow plane selection.

The minimum particle size is dependant on the size of the field of view and the resolution of the camera, i.e. the particles need to be large enough to produce shadow spots on the images with back-light illumination. In practice this means that the particle sizes used in shadow PIV generally needs to be larger than for laser PIV. Larger particles are less likely to follow the flow and behave as tracers, however the Stokes number analysis in Methods section 2.2 showed that our 40 μm particles have a Stokes number significantly smaller than 0.1 which should give an acceptable flow tracing accuracy with errors less than 1% [39].

Accurate flow plane definition is also a challenge with a shadow PIV setup. In laser PIV, the thickness of the illumination plane can be can be very thin and the position of the plane can be accurately prescribed, giving good control of the spatial coordinates of the measured flow velocities. In our setup the flow is presumed to be predominantly 2D because of the shallow depth of the flow domain compared to the in plane axes (x and y-directions, as given in Figs. 1 and 4), in addition all planes in the in depth direction have the same geometry. Because of these considerations a deep depth-of-field was chosen to cover a large part of the flow domain in the out of plane direction, more precisely the depth-of-field was set to approximately 5 mm in the center of the 7 mm deep flow domain. This means that the particles seen in the particle flow images are a composite of all particles within the depth-of-field region. The particle flow images are the data basis for the window correlation post-processing to calculate the velocity components of the flow, hence significant velocity changes in the depth direction will introduce errors in the estimation of the in plane velocity field, since the output from the window correlation at a specific area is determined by the correlation signal with the highest signal magnitude, i.e. within the entire depth-of-field and not at a specific plane. However for our case, the flow especially during systole showed to be highly 2D in nature giving us high confidence that our PIV velocity component estimates represent the true in plane flow field.

5. Conclusion

In conclusion, our results show that there is generally good agreements between the three modalities, especially when integrated quantities of the flow are compared such as volumetric flow rate and flow field maximum velocities. However, the US flow reconstruction results in an under estimation of the flow velocity magnitude and curl intensity when compared to PIV and CFD. The CFD results compares very well with the PIV flow field maximum velocities and curl intensity. The key vortical structures are captured by both US and CFD but need to be interpreted with the characteristics of the two methods in mind. CFD results represent a snap shot over a shorter time frame and different depth of field compared to US and PIV (the CFD results are averaged over three plans over the cross section) and retains the characteristics of a global shutter. In our setup the PIV employs a global shutter, and effectively averages over most of the cross section of the flow with its 5 mm depth of field. The under estimation produced by US is due to regularization and aliasing, and the US setup employs a rolling shutter.

In our view, regularized US shows great promise for characterizing biomedical flows in less idealized settings than our in-vitro setup, and that such imaging and data enhancing methods and CFD models interacting through the exchange of data for high quality boundary conditions and model verification will be a path towards wider clinical use of computational methods for flow characterization and decision support. Not surprisingly, attention to time and volume averaging is important, and knowledge of how to interpret data obtained from the three modalities US, PIV and CFD is essential when making comparisons or clinical interpretations.

Declaration of competing interest

Morten Smedsrud Wigen has previously had a part-time consultancy at GE Vingmed Ultrasound.

Acknowledgement

This study was internally funded by SINTEF and the Norwegian University of Science and Technology (NTNU) and supported by the Center for Innovative Ultrasound Solutions (CIUS) through funding from the Research Council of Norway (grant number 237887)

Appendix A. Supplementary data

Supplementary data to this article can be found online at https://doi.org/10.1016/j.compbiomed.2022.105358.

References

[1] Ronald J. Adrian, Particle-Imaging techniques for experimental fluid mechanics, Annu. Rev. Fluid Mech. 23 (1) (1991) 261–304, https://doi.org/10.1146/annurev.fl.23.010191.001401. (Accessed 17 November 2019).

[2] Ronald J. Adrian, Chung-Sheng Yao, Pulsed laser technique application to liquid and gaseous flows and the scattering power of seed materials". EN, Appl. Opt. 24.1 (Jan. 1985) 44–52, https://doi.org/10.1364/AO.24.000044. Publisher: Optical Society of America, issn: 2155-3165. (Accessed 11 November 2020).

[3] Arshid Azarine, Philippe Garçon, Audrey Stansal, Nadia Canepa, Giorgios Angelopoulos, Stephane Silvera, Daniel Sidi, VeroniqueMarteau, Marc Zins, Four-dimensional flow MRI: principles and cardiovascular applications, Radiographics 39 (3) (2019) 632–648.

[4] Pinaki Chakraborty, S. Balachandar, Ronald J. Adrian, On the relationships between local vortex identification schemes, J. Fluid Mech. 535 (2005) 189–214.

[5] Laurence Joseph Clancy, Aerodynamics, John Wiley & Sons, 1975.

[6] Brent A. Craven, Kenneth I. Aycock, Keefe B. Manning, Steady flow in a patient-averaged inferior vena cava-Part II: computational fluid dynamics verification and validation, Cardiovasc. Eng. Technol. 9 (4) (Dec. 2018) 654–673, https://doi.org/10.1007/s13239-018-00392-0.

[7] Sigrid Kaarstad Dahl, Numerical Simulations of Blood Flow in the Left Side of the Heart, PhD thesis, 2012.

[8] Jordi Estevadeordal, Larry Goss, PIV with LED: particle shadow velocimetry (PSV) technique, in: *43rd AIAA Aerospace Sciences Meeting and Exhibit*. 43rd AIAA Aerospace Sciences Meeting and Exhibit, American Institute of Aeronautics and Astronautics, Reno, Nevada, Jan. 10, 2005, ISBN 978-1-62410-064-2, https://doi.org/10.2514/6.2005-37. (Accessed 16 November 2019).

[9] S. Fadnes, S. Bjærum, H. Torp, L. Lovstakken, Clutter filtering influence on blood velocity estimation using speckle tracking, IEEE Trans. Ultrason. Ferroelectrics Freq. Control 62 (12) (2015) 2079–2091, https://doi.org/10.1109/TUFFC.2015.007247.

[10] Solveig Fadnes, Morten S. Wigen, Siri Ann Nyrnes, Lasse Lovstakken, In vivo intracardiac vector flow imaging using phased array transducers for pediatric cardiology, IEEE Trans. Ultrason. Ferroelectrics Freq. Control 64 (9) (2017) 1318–1326.

[11] Matthew D. Ford, Hristo N. Nikolov, Jaques S. Milner, Stephen P. Lownie, Edwin M. DeMont, Wojciech Kalata, Francis Loth, David W. Holdsworth, David A. Steinman, PIV-measured versus CFD-predicted flow dynamics in anatomically realistic cerebral aneurysm models, J. Biomech. Eng. 130 (2) (2008).

[12] Prasanna Hariharan, Kenneth I. Aycock, Martin Buesen, Steven W. Day, Bryan C. Good, Luke H. Herbertson, Ulrich Steinseifer, Keefe B. Manning, Brent A. Craven, Richard A. Malinauskas, Inter-laboratory characterization of the velocity field in the FDA blood pump model using particle image velocimetry (PIV), Cardiovasc. Eng. Technol. 9 (4) (Dec. 2018) 623–640, https://doi.org/10.1007/s13239-018-00378-y.21.

[13] Prasanna Hariharan, Gavin A. D'Souza, Marc Horner, Tina M. Morrison, Richard A. Malinauskas, Matthew R. Myers, Use of the FDA nozzle model to illustrate validation techniques in computational fluid dynamics (CFD) simulations, PLoS One 12 (6) (2017), e0178749, https://doi.org/10.1371/journal.pone.0178749.

[14] David Hasler, Andrin Landolt, Dominik Obrist, Tomographic PIV behind a prosthetic heart valve, Exp. Fluid 57 (5) (2016) 80.

[15] Seyed Ali Hosseini, Philipp Berg, Feng Huang, Christoph Roloff, Gábor Janiga, Dominique Thávenin, Central moments multiple relaxation time LBM for hemodynamic simulations in intracranial aneurysms: an in-vitro validation study using PIV and PC-MRI, Comput. Biol. Med. 131 (2021), 104251.

[16] R. Israel, Daniel E. Rosner, Use of a generalized Stokes number to determine the aerodynamic capture efficiency of non-Stokesian particles from a compressible gas flow, Aerosol. Sci. Technol. 2 (1) (1982) 45–51.

[17] Jinhee Jeong, Fazle Hussain, On the identification of a vortex, J. Fluid Mech. 285 (1995) 69–94.

[18] Christian J. Kahler, Sven Scharnowski, Christian Cierpka, On the resolution limit of digital particle image velocimetry, Exp. Fluid 52 (6) (June 2012) 1629–1639, https://doi.org/10.1007/s00348-012-1280-x, issn: 1432-1114. (Accessed 13 October 2020).

[19] Paul R. Leinan, Skjetne Paal, John Morud, Stig Urheim, Sigrid Kaarstad Dahl, Velocity profiles in a 2D model of the left ventricular outflow tract, pathological case study using PIV and CFD modeling, in: Progress in Applied CFD–Cfd2017 Selected Papers from 12th International Conference on Computational Fluid Dynamics in the Oil & Gas, Metallurgical and Process Industries, SINTEF akademisk forlag, 2017.

[20] Richard A. Malinauskas, Prasanna Hariharan, Steven W. Day, Luke H. Herbertson, Martin Buesen, Ulrich Steinseifer, Kenneth I. Aycock, Bryan C. Good, Steven Deutsch, Keefe B. Manning, and Brent A. Craven. "FDA benchmark medical device flow models for CFD validation." In: Am. Soc. Artif. Intern. Organs J. 63.2, pp. 150–160.

[21] Anders Koustrup Niemann, Samuel Thrysoe, Jens Vinge Nygaard, John Michael Hasenkam, Steffen Ellebaek Petersen, Computational fluid dynamics simulation of av fistulas: from MRI and ultrasound scans to numeric evaluation of hemodynamics, J. Vasc. Access 13 (1) (2012) 36–44.

[22] Siri A. Nyrnes, Solveig Fadnes, Morten S. Wigen, Luc Mertens, Lasse Lovstakken, Blood speckle-tracking based on high–frame rate ultrasound imaging in pediatric cardiology, J. Am. Soc. Echocardiogr. 33 (4) (2020) 493–503, https://doi.org/10.1016/j.echo.2019.11.003, e5. issn: 0894-7317.

[23] Nikhil Paliwal, Robert J. Damiano, Nicole A. Varble, Vincent M. Tutino, Zhongwang Dou, Adnan H. Siddiqui, Meng Hui, Methodology for computational fluid dynamic validation for medical use: application to intracranial aneurysm, J. Biomech. Eng. 139 (2017) 12.

[24] Jaime S. Raben, Prasanna Hariharan, Ronald Robinson, Richard Malinauskas, Pavlos P. Vlachos, Time-resolved particle image velocimetry measurements with wall shear stress and uncertainty quantification for the FDA nozzle model, Cardiovasc. Eng. Technol. 7 (1) (Mar. 2016) 7–22, https://doi.org/10.1007/s13239-015-0251-9.22.

[25] Thomas A. Roberts, Joshua F.P. van Amerom, Alena Uus, David F.A. Lloyd, Milou P.M. van Poppel, Anthony N. Price, Jacques-Donald Tournier, Chloe A. Mohanadass, Laurence H. Jackson, Shaihan J. Malik, Kuberan Pushparajah, Mary A. Rutherford, Reza Razavi, Maria Deprez, Joseph V. Hajnal, Fetal whole heart blood flow imaging using 4D cine MRI, Nat. Commun. 11 (1) (Oct. 2020) 4992, issn: 2041-1723.

[26] Bodo Ruck, Einfluß der Tracerteilchengröße auf die Signalinformation in der Laser-Doppler-Anemometrie/Influence of tracer particle size on flow information in laser Doppler anemometry, in: Tm-Technisches Messen, vol. 57, 1990, pp. 284–295. JG.

[27] Hicham Saaid, Jason Voorneveld, Christiaan Schinkel, Jos Westenberg, Gijsen Frank, Segers Patrick, Verdonck Pascal, Nico de Jong, Johan G. Bosch, Sasa Kenjeres, Claessense Tom, Tomographic PIV in a model of the left ventricle: 3D flow past biological and mechanical heart valves, J. Biomech. 90 (2019) 40–49.

[28] F. Scarano, Theory of non-isotropic spatial resolution in PIV, en, Exp. Fluid 35 (3) (Sept. 2003) 268–277, https://doi.org/10.1007/s00348-003-0655-4. issn: 0723-4864, 1432-1114. (Accessed 11 November 2020).

[29] K.J.M. Surry, H.J.B. Austin, A. Fenster, T.M. Peters, Poly (vinyl alcohol) cryogel phantoms for use in ultrasound and MR imaging, Phys. Med. Biol. 49 (24) (2004) 5529.

[30] Abigail Swillens, Joris Degroote, Jan Vierendeels, Lasse Lovstakken, Patrick Segers, A simulation environment for validating ultrasonic blood flow and vessel wall imaging based on fluid-structure interaction simulations: ultrasonic assessment of arterial distension and wall shear rate, Med. Phys. 37 (8) (2010) 4318–4330.

[31] Sean Guo-Dong Tan, Sangho Kim, Jimmy Kim Fatt Hon, Hwa Liang Leo, A D-shaped bileaflet bioprosthesis which replicates physiological left ventricular flow patterns, PLoS One 11 (6) (2016), e0156580.

[32] Joshua O. Taylor, Bryan C. Good, Anthony V. Paterno, Prasanna Hariharan, Steven Deutsch, Richard A. Malinauskas, Keefe B. Manning, Analysis of transitional and turbulent flow through the FDA benchmark nozzle model using laser Doppler velocimetry, Cardiovasc. Eng. Technol. 7 (3) (Sept. 2016) 191–209, https://doi.org/10.1007/s13239-016-0270-1.

[33] William Thielicke, Eize Stamhuis, PIVlab–towards user-friendly, affordable and accurate digital particle image velocimetry in MATLAB, J. Open Res. Software 2 (1) (2014).

[34] Cameron Tropea, Alexander L. Yarin, John F. Foss, Springer Handbook of Experimental Fluid Mechanics, vol. 1, Springer Science & Business Media, 2007.

[35] Joris Van Cauwenberge, Lasse Lovstakken, Solveig Fadnes, Alfonso Rodriguez-Morales, Jan Vierendeels, Patrick Segers, Abigail Swillens, Assessing the performance of ultrafast vector flow imaging in the neonatal heart via multiphysics modeling and in vitro experiments, IEEE Trans. Ultrason. Ferroelectrics Freq. Control 63 (11) (2016) 1772–1785, 23.

[36] Marco Viceconti, Miguel A. Juarez, Cristina Curreli, Marzio Pennisi, Giulia Russo, Francesco Pappalardo, Credibility of in silico trial technologies-A theoretical framing, IEEE J. Biomed. Health Inf. 24 (1) (Jan. 2020) 4–13, https://doi.org/10.1109/JBHI.2019.2949888.

[37] Jerry Westerweel, Fulvio Scarano, Universal outlier detection for PIV data, Exp. Fluid 39 (6) (Dec. 2005) 1096–1100, https://doi.org/10.1007/s00348-005-0016-6, issn: 1432-1114. (Accessed 10 December 2020).

[38] M.S. Wigen, S. Fadnes, A. Rodriguez-Molares, T. Bjastad, M. Eriksen, K. H. Stensæth, A. Støylen, L. Lovstakken, 4-D intracardiac ultrasound vector flow imaging–feasibility and comparison to phase-contrast MRI, IEEE Trans. Med. Imag. 37 (12) (2018) 2619–2629, https://doi.org/10.1109/TMI.2018.2844552.

[39] Hui Zhou, Long Meng, Wei Zhou, Xin Lin, Xiangxiang Xia, Shuai Li, Hairong Zheng, Lili Niu, Computational and experimental assessment of influences of hemodynamic shear stress on carotid plaque, Biomed. Eng. Online 16 (1) (2017) 1–11, 24.